Theoretical exploration of laser-parameter effects on the generation of an isolated attosecond pulse from two-color high-order harmonic generation

Tianjiao Shao,[1,2] Guangjiu Zhao,[1,3,*] Bin Wen,[2] and Huan Yang[1,3]

[1]*State Key Laboratory of Molecular Reaction Dynamics, Dalian Institute of Chemical Physics,*
Chinese Academy of Sciences, Dalian 116023, China
[2]*School of Materials Science and Engineering, Dalian University of Technology, Dalian 116024, China*
[3]*School of Physics, Shandong University, Jinan 250100, China*

In the present work, laser-parameter effects on the isolated attosecond pulse generation from two-color high-order harmonic generation (HHG) process are theoretically investigated by use of a wave-packet dynamics method. A 6-fs, 800-nm, 6×10^{14} W/cm^2, linearly polarized laser pulse serves as the fundamental driving pulse and parallel linearly polarized control pulses at 400 nm (second harmonic) and 1600 nm (half harmonic) are superimposed to create a two-color field. Of the two techniques, we demonstrate that using a half-harmonic control pulse with a large relative strength and zero phase shift relative to the fundamental pulse is a more promising way to generate the shortest attosecond pulses. As a consequence, an isolated 12-as pulse is obtained by Fourier transforming an ultrabroad xuv continuum of 300 eV in the HHG spectrum under half-harmonic control scheme when the relative strength $\sqrt{R} = 0.6$ and relative phase $= 0$.

I. INTRODUCTION

Emergence of the attosecond (as) laser pulse has enabled researchers to observe and control the ultrafast atomic-level and subatomic-level dynamics with unprecedented accuracy and resolution [1–3]. These ultrashort pulses can be generated in several approaches, such as Fourier synthesis of Raman sidebands [4], or by using the process of high-order harmonic generation (HHG) in noble gases [5].

To date, isolated attosecond xuv pulses have been experimentally generated using two techniques: temporal confinement of the HHG by polarization gating or a few-cycle driving pulse. The main advantage of the polarization-gating technique is that it is simpler to realize in the laboratory [6–12]. Using the few-cycle laser-pulse technique, Sansone *et al.* have obtained a single 130-as pulse generated from a 36-eV continuum after compensating for the harmonic chirp [6]. Recently, an isolated 80-as pulse of xuv light was obtained in experiments [13].

It should be noted that it is difficult to generate attosecond pulses with durations less than 100 as with the few-cycle laser pulse technique due to the limited duration of the driving pulse. Hence, this issue was addressed by using a two-color laser field with a controlled wave form [8–31]. Zeng *et al.* superposed a weak second harmonic control pulse onto an intense few-cycle fundamental pulse with an optimized phase and a 148-eV continuum supporting a 65-as isolated pulse was predicted [14]. Recently, Merdji *et al.* also proposed a method to generate isolated attosecond pulses using a two-color scheme composed of multicycle pulses with comparable intensity [15]. Kim and co-workers reported another approach. A weak pulse in the ir region was added upon a multicycle 800-nm pulse and an isolated attosecond pulse was predicted [16]. Mauritsson *et al.* compared the effect of symmetry breaking under the two-color scheme and revealed subcycle control of an attosecond pulse [17]. Recently, Liu *et al.* proposed a

method to create an isolated 39-as pulse by adding a xuv pulse upon the synthesized two-color field at a proper time [25,26]. In addition, a control field with a different wavelength, such as uv pulse, half-harmonic pulse, and electrostatic field superposed on an intense 800-nm pulse, have also been intensively investigated [19–24].

Very recently, a parallel quantum electron-and-nuclei wave-packet dynamics program has been developed by Han and co-workers to investigate the laser-atom-molecule interaction in the nonperturbative regime with attosecond resolution by numerically solving the time-dependent Schrödinger equation of electrons and nuclei [32–40]. Time propagation of the wave functions is performed using a split-operator approach and based on a sine discrete variable representation. By performing this code, Guo *et al.* propose a scheme in which the driving pulse is modulated by a half-harmonic control pulse, a continuum with bandwidth more than 300 eV supporting a 53-as pulse was obtained [32]. In addition, Lu *et al.* proposed a three-color field scheme in which an effect of a 3-fs driving field is achieved by utilizing two weak pulses to modify a fundamental one [33].

We report a detailed investigation on parameter effects induced by control pulse frequency, relative phase, and relative strength ratio here. It is noteworthy that among all the techniques based on the HHG process, Carrier envelope phase (CEP) stabilization is an important prerequisite. All the schemes in our simulation are based on the assumption that the CEP of the pulse used is locked to zero for simplifying the discussion.

II. THEORETICAL METHOD

In our numerical simulations, both the HHG spectrum and the isolated attosecond pulse are obtained by solving the following time-dependent Schrödinger equation based on single-active electron approximation via the parallel quantum wave-packet computer code LZH-DICP. In this program, the

---

*attophys@126.com

sine discrete variable representation (DVR) and split-operator method are used to numerically solve the time-dependent Schrödinger equation (TDSE) [32–40].

The Schrödinger equation has the expression

$$i\frac{\partial}{\partial t}\Psi(r,t) = \hat{H}\Psi(r,t) = [\hat{H}_0 + \hat{V}(r,t)]\Psi(r,t), \qquad (1)$$

where $\hat{H}_0$ is the field-free Hamiltonian, $\hat{H}_0 = T + V = -\frac{1}{2}\nabla^2 + V_C$; V_C is the Coulomb potential; and $V(r,t)$ defines the interaction potential between the atom and the strong electric field, $V(r,t) = rE(t)$.

The time-dependent wave function is advanced using the standard second-order split-operator method:

$$\Psi(t+\delta t) = e^{-iT\delta t/2}e^{-iV\delta t}e^{-iT\delta t/2}\Psi(t) + O(\delta t^3), \qquad (2)$$

where T is the kinetic-energy operator and V is the interaction potential. All the potential energy of the system is taken into account, plus a purely imaginary term to produce an absorbing boundary.

After determining the time-dependent wave function, we can calculate the time-dependent induced dipole acceleration according to the Ehrenfest theorem as

$$d_A(t) = \langle\Psi(r,t)|-\frac{V(r,t)}{r}|\Psi(r,t)\rangle$$
$$= \langle\Psi(r,t)|-\frac{V_C}{r} + E(t)|\Psi(r,t).\rangle \qquad (3)$$

Then, harmonic spectra [i.e., Figs. 1(b), 1(d), 1(f)] are obtained by Fourier transforming the time-dependent dipole acceleration:

$$P_A(w) = \left|\frac{1}{\sqrt{2\pi}}\int d(t)e^{-i^*w^*t}dt\right|^2. \qquad (4)$$

In our work, the gas medium used in the simulation is helium (He). He as a typical noble gas medium in attosecond pulse generation can be approximated as a one-electron system providing a robust HHG spectra to support our results. A soft-core potential of helium is applied with the formula: $V(x) = -1/\sqrt{a+x^2}$. The parameter a equal to 0.484 is chosen, so that the ionization energy I_p of 24.6 eV corresponds to the ground state of helium, which matches the experimental value. A 6-fs, 800-nm, 6×10^{14} W/cm^2 pulse serves as the fundamental field for generating attosecond pulses. In addition, the duration of the control pulses discussed are all chosen to be 12 fs since this parameter plays a minor role in simulation.

The fundamental pulse (FP) alone can be expressed as

$$E(t) = E_0 \exp\left[-4\ln(2)t^2/\tau_0^2\right]\cos(w_0 t). \qquad (5)$$

The synthesized electric field can be expressed as

$$E(t) = E_0\big\{\exp\left[-4\ln(2)t^2/\tau_0^2\right]\cos(w_0 t)$$
$$+ \sqrt{R}\exp\left[-4\ln(2)(t+\Delta t)^2/\tau_1^2\right]\cos[w_1(t+\Delta t)]\big\}, \qquad (6)$$

$$\text{phase} = 2\pi\frac{\Delta t}{T_1} = w_1\Delta t. \qquad (7)$$
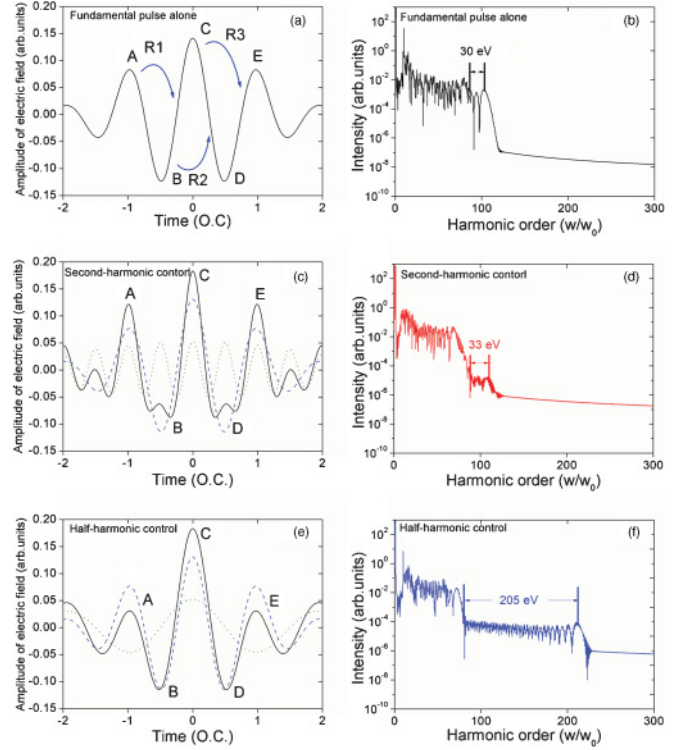
FIG. 1. (Color online) Electric fields are displayed in the left column (time is in units of optical cycles of 800-nm pulses in all the plots of electric fields), and the generated corresponding HHG spectra are shown in the right column. Laser parameters in the simulation are as follows. (a), (b) Fundamental laser pulse, 800 nm, 6 fs, 7×10^{14} W/cm^2; no control pulse. (c), (d) Fundamental pulse, 800 nm, 6 fs, 6×10^{14} W/cm^2; control pulse, 400 nm, 12 fs, $\sqrt{R} = 0.4$, phase = 0. (e), (f) Fundamental pulse, 800 nm, 6 fs, 6×10^{14} W/cm^2; control pulse, 1600 nm, 12 fs, $\sqrt{R} = 0.4$, phase = 0.

The relative strength ratio of the control pulse (CP) can be expressed as

$$\sqrt{R} = \frac{E_1}{E_0} = \sqrt{\frac{I_1}{I_0}}. \qquad (8)$$

The Gaussian pulse envelope is chosen, with the formula

$$f(t) = \exp[-4\ln(2)t^2/\tau^2]. \qquad (9)$$

In the preceding equations, w_0, w_1 are the frequencies of the FP and the CP, respectively; E_0, E_1 are the electric field amplitudes; τ_0, τ_1 are the corresponding pulse durations (FWHM). Fig 1(a) shows the 6-fs, 800-nm, 7×10^{14} W/cm^2 FP alone without CP, while Figs. 1(c) and 1(e) depict the synthesized field by FP with its second harmonic CP and half-harmonic CP, respectively.

III. RESULTS AND DISCUSSIONS

A. Control schemes effect

To understand HHG's dependence on control pulse frequency, the HHG processes are first analyzed by analyzing profile of the driving field. We analyze the HHG process in terms of the well-known three-step model [41,42]. According to this model, as shown by Fig. 1(a), first the atoms are ionized

and the electrons are ejected around the first peak labeled as A through tunneling ionization, then they are accelerated by the following peak B, and finally recombine with the ions between the B and C peaks. This process has a period of half optic cycle of the pulse. In each half-cycle emission, maximum frequency of the emitted photons is referred to the cutoff frequency. The few-cycle pulse shown by Fig. 1(a) owns five peaks labeled as A, B, C, D, and E, respectively. Consequently, there will be three independent periodical processes: A to B to C, B to C to D, and C to D to E; three unique cutoffs will emerge on the HHG spectrum correspondingly. The concept of continuum is defined as a spread of harmonics with their frequency between the largest cutoff energy and the second largest cutoff energy. From the above analyses, the first peak A determines the ionizing process; the second peak B determines the accelerating process. As a result, the former peak determines the harmonic efficiency, while the latter one determines the location of the cutoff frequency on HHG spectra. Therefore, we can expect that the intensity of the emitted harmonics could be improved by increasing the first peak, while the cutoff with larger harmonic order would be achieved by increasing the second peak.

The frequency of the CP plays an important role in modulating the HHG process. Figures 1(a), 1(c), and 1(e) show the electric field of a 6-fs few-cycle pulse alone with intensity of 7×10^{14} W/cm^2; two-color field with a FP of 6 fs, 6×10^{14} W/cm^2, and a second-harmonic CP with its intensity 0.96×10^{14} W/cm^2; and a half-harmonic CP with its intensity 0.96×10^{14} W/cm^2, respectively. To simplify discussion, all graphs in Fig. 1 are controlled by the symmetrical electric fields in which the heights of peaks B and D are equivalent. Thus, the location of the cutoff from the emission event of "A to B to C" and "C to D to E" should be same. As a consequence, we only need to focus on discussion of the cutoff from the emission event of "A to B to C" and "B to C to D." Figures 1(b), 1(d), and 1(f) show the HHG spectrum generated by the three kinds of fields, respectively.

As shown by Fig. 1(f), an ultrabroad spectral width of 215 eV is achieved under the half-harmonic control, which is much larger than the other two cases of 30 and 33 eV, respectively. The 30-eV continuum is reported for producing a 250-as pulse [43]. However, a sub-100-as pulse can only rely on a broader continuum, such as those generated by half-harmonic control mentioned earlier.

As shown in Fig. 1(e), superposing a half-harmonic decreases the height of A and E and increases the height of the peak C, while keeping peaks B and peak D invariable. Therefore, we can expect qualitatively that the process of "A to B to C" will emit harmonics with lower intensity, whereas the process of "B to C to D" will radiate photons with larger cutoff energy and with their efficiency invariable. A continuum is defined as the harmonics between the second-largest cutoff and the largest cutoff. Thus, it is favorable to see that the yields of the useless harmonics before the second-largest cutoff decreased and the width of continuum is broadened. To understand the physics behind the broadened continuum under a half-harmonic control field, time-frequency analyses are performed to transform the dipole responses of the He atom of the preceding three cases [44–49]. Wavelet Fourier is applied to transform the dipole acceleration, which is taken as
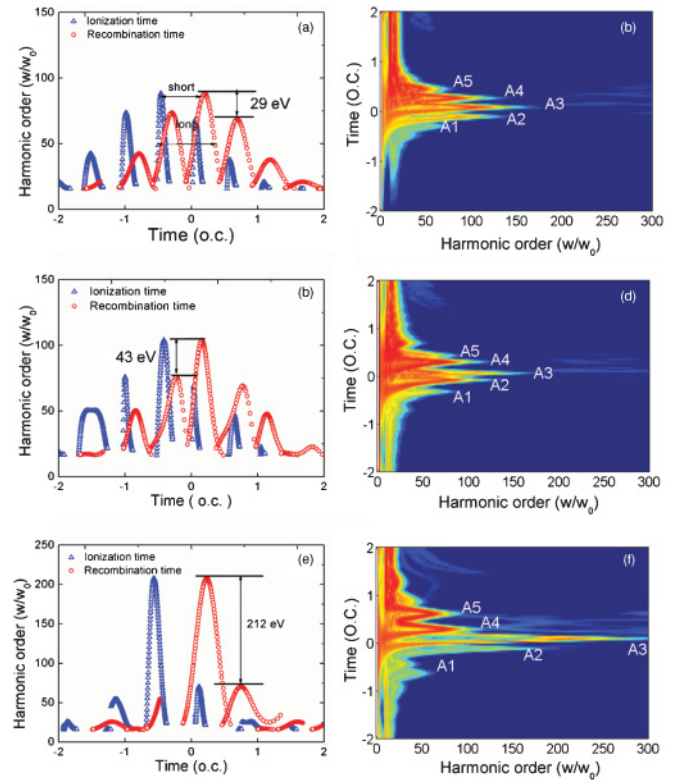
FIG. 2. (Color online) Classical returning-kinetic-energy maps are shown in the left column (time is in units of optical cycles of 800-nm pulse in all the classical returning-kinetic-energy maps), and time-frequency analyses of the HHG power spectra generated (colors in logarithmic scale) are displayed in the right column (time is in units of femtoseconds in all the time-frequency analyses). Laser parameters in the simulation are as follows. (a), (b) Fundamental laser pulse, 800 nm 6 fs 7×10^{14} W/cm^2; no control pulse. (c), (d) Fundamental pulse, 800 nm 6 fs 6×10^{14} W/cm^2; control pulse, 400 nm, 12 fs, $\sqrt{R} = 0.4$, phase $= 0$. (e), (f) Fundamental pulse, 800 nm, 6 fs 6×10^{14} W/cm^2; control pulse, 1600 nm, 12 fs, $\sqrt{R} = 0.4$, phase $= 0$.

the expression

$$d_w(t) = \int d(t) w_{t_0,w}(t) \, dt. \tag{10}$$

The wavelet kernel is chosen to be the Morlet wavelet [50]

$$
\begin{aligned}
w_{t_0,w}(x) &= \sqrt{w} W[w(t - t_0)], \\
W(x) &= (1/\sqrt{\tau}) e^{ix} e^{-x^2/2\tau^2}.
\end{aligned}
\tag{11}
$$

In the following, we choose $\tau = 15$ to perform the wavelet transform, which corresponds to the time window of $15w_0$. As shown by the Figs. 2(b), 2(d), and 2(f), the color scale represents the intensity of the photons, which is the function of the harmonic order at the horizontal axis and the time of emission at the vertical axis. In particular, we focus our attention on the five emission bursts labeled from A1 to A5. These five peaks indicate the maximum emitted energy of the returning electrons, as well as their recombination times in each half-cycle emission. In Figs. 2(b) and 2(d), either the height of the largest peak, A3, or the cutoff energy difference between peaks A3 and A2 is smaller compared

with Fig. 2(f), which strongly limits the continuum width on the HHG spectra. When the FP are superposed by the half-harmonic CP with a zero time delay, the height of peak A3 is significantly increased, whereas the heights of the neighboring two peaks, A2 and A4, are nearly invariable. As a result, the enlarged energy difference between peaks A3 and A2 induce the extension of the continuum width on the HHG spectra.

Classical returning kinetic-energy maps are used for detailed discussion. Figures 2(a), 2(c), and 2(e) depict a larger number of trajectories with a given velocity. Each dot in the classical returning kinetic-energy map corresponds to an emission event with definite harmonic order on the HHG spectrum. The density of the points reflects the intensity of the harmonics. It is well known, in the HHG process, that a path with earlier ionization time but later recombination time is defined as a long trajectory, while a path with later emission time but earlier recombination time is named as a short trajectory. It is worth noting that the HHG spectra in our work shown in Figs. 1, 3, and 5 are all based on the emissions from both short and long trajectories. The interference between the short and the long trajectories results in phase-dependent modulation on HHG spectra, which we discuss later. The phenomenon that symbols representing short trajectories are usually more intense than those representing long trajectories implies that high-order harmonic generation is mainly based on short trajectories. These results were also shown theoretically [51] and experimentally [52] in the previous works. As shown in the classical returning kinetic-energy map, the cutoff energy difference between the neighboring emission events is enhanced to 205 eV when the driving field is modulated by the half-harmonic CP, compared with the 30 and 33 eV in the other two cases, respectively. This is consistent with the preceding time-frequency analyses.

Consistent results from both quantum and classical simulation indicate that half-harmonic control is a more promising approach to broadening the continuum on HHG spectra. Hence, only the half-harmonic control scheme is discussed in the following discussion.

B. The phase effect

Previous studies have showed that the phase between the FP and the CP could break the half-cycle emission into one-cycle emission [53,54]. Moreover, relative phase plays a role in shaping the wave form of the synthesized field, thus significantly modulating the electron's trajectory. Herein, by varying the phase between the FP and the CP, the HHG process's dependence on relative phase is investigated.

Figure 3(a) is a 3D graph in which the color represents the intensity of the harmonics, which is the function of the harmonic order and the relative phase between FP and CP. In the simulation, we fix $\sqrt{R}$ to be 0.4, and the phase between two pulses varies from $-\pi$ to π in each $\pi/8$ rad. The furthest cutoff of 215 is achieved when the phase is zero. The cases when the relative phase is $\pi/4$, $\pi/8$, 0, $-\pi/8$ are labeled with blue dashed-dotted line, red dotted line, black solid line, green dashed line, respectively, in Fig. 3(a). In Fig. 3(b), HHG spectra when the relative phase is $\pi/4$, $\pi/8$, 0, and $-\pi/8$ are plotted
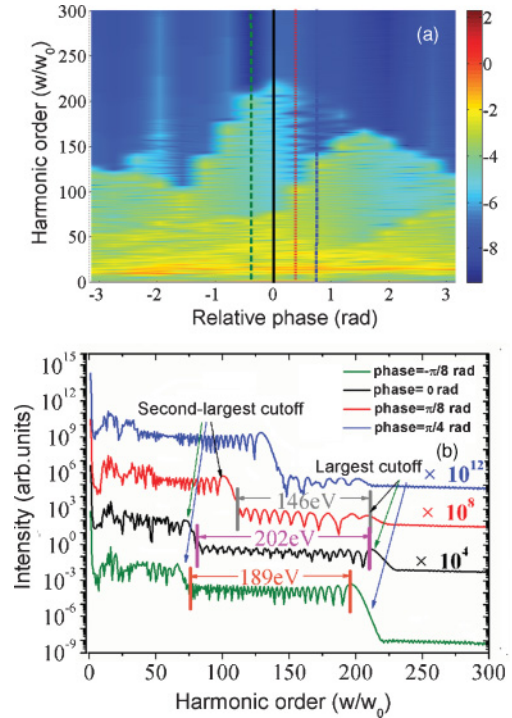
FIG. 3. (Color online) (a) Photon energies as a function of relative phase (a calculated scan). The blue dash-dotted line, red dotted line, black solid line, and green dashed line represent, respectively, the cases when phase is $\pi/4$, $\pi/8$, 0, and $-\pi/8$. (b) HHG spectra taken at the phases $\pi/4$, $\pi/8$, 0, $-\pi/8$, marked with blue, red, black, and green lines, respectively, from top to bottom. In all four cases, $\sqrt{R} = 0.4$.

from top to bottom, respectively. As shown by Fig. 3(b), the continuum of the HHG spectrum with the zero phase shift is wider than the other three cases. When the phase changes from $\pi/8$ to zero, the largest cutoff remains almost invariable, while the second-largest cutoff shifts to the lower order. A 202-eV continuum when phase shift is around zero is larger than the case of $-\pi/8$ phase's 189 eV and $\pi/8$ phase's 146 eV for 13 and 56 eV, respectively. This again shows that the HHG process is sensitive to the laser parameter. Consequently, our results indicate zero phase shift between FP and CP should be chosen in order to obtain widest spectral width on the HHG spectrum under half-harmonic control.

To reveal the physical picture behind the relative phase effects, in Fig. 4, the specific case when phase = $\pi/8$ is investigated by time-frequency analyses and classical trajectory simulation to compare with its corresponding half-harmonic control case shown in Figs. 1 and 2, where all the laser parameters are the same except a relative phase shift of zero. In Fig. 2(e), when phase = 0, there are three main peaks, the main peak B is much higher than adjacent peaks for 212 eV. In Fig. 4(b), when phase = $\pi/8$, there are only two high peaks in the classical returning kinetic-energy map. The energy difference between the two peaks is around 161 eV, which leads to a shorter continuum on the HHG spectra. Figure 4(c) is the quantum time-frequency analysis which provides consistent information with the corresponding classical returning kinetic-energy map.
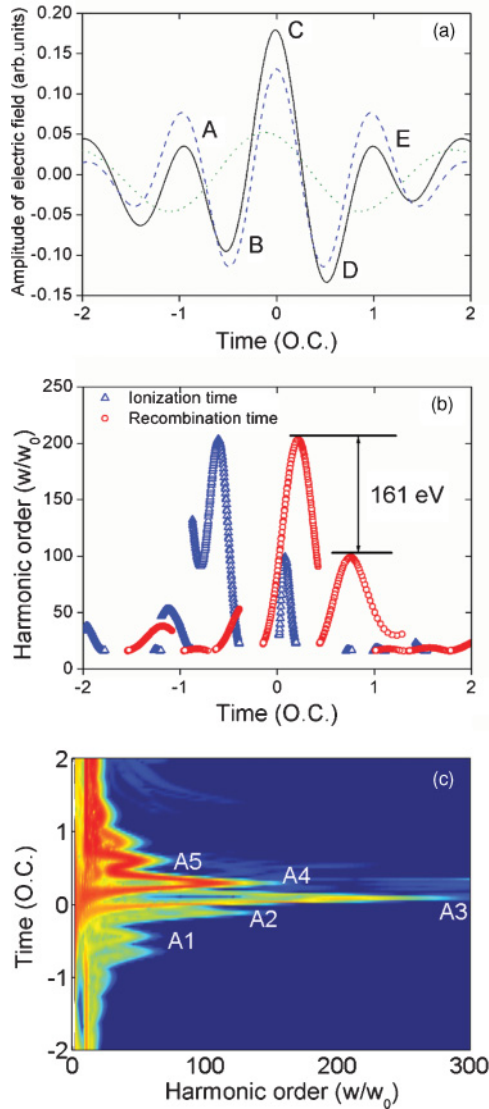
FIG. 4. (Color online) (a) Profile of electric field when phase is $\pi/8$. (b) Classical returning-kinetic-energy maps. (c) Time-frequency profile (colors are in logarithmic scale) of the HHG power spectra. Laser parameters in the simulation are as follows. Fundamental pulse, $800\,\text{nm}\,6\,\text{fs}\,6\times10^{14}\,\text{W/cm}^2$; control pulse, $1600\,\text{nm}$, $12\,\text{fs}$, $\sqrt{R}=0.4$, phase $=\pi/8$.

C. The relative strength effect

The relative strength ratio of CP also plays an important role in shaping the wave form of the synthesized field [55]. On account of the preceding discussion, we fix the phase to be 0 and vary the relative strength ratio $\sqrt{R}$ to investigate the HHG process's dependence on $\sqrt{R}$. In Fig. 5(a), the dependence of both the largest cutoff and the second-largest cutoff on the relative phase are shown by performing classical trajectory simulation. The second-largest cutoff increases slightly by varying the $\sqrt{R}$ and its value is always within the range of 76 and 105 (in the measurement of harmonic order). However, this is not the case with the largest cutoff; the largest cutoff is sensitive to the change of $\sqrt{R}$ and increases linearly with the augment of $\sqrt{R}$, as can be seen in Fig. 5(a). From the profile of the electric field shown in Fig. 1(d), we may obtain a qualitative
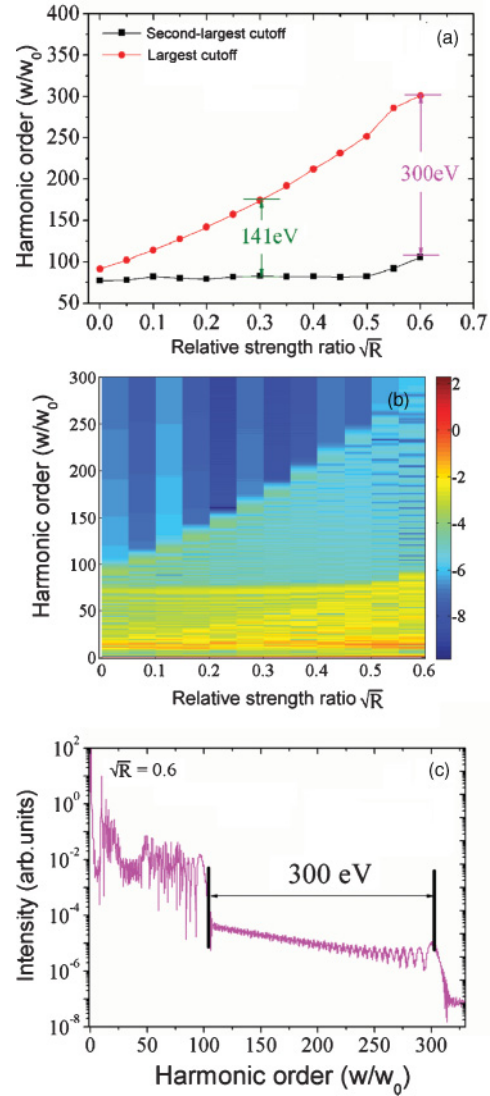
FIG. 5. (Color online) (a) Harmonic cutoffs as a function of relative strength ratio $\sqrt{R}$ obtained by classical trajectory simulation. (b) Photon energies as a function of strength ratio $\sqrt{R}$ (colors are in logarithmic scale). (c) HHG spectra by the half-harmonic control when $\sqrt{R}=0.6$.

explanation. Under half-harmonic control, peak C is enhanced, peak B is invariable, and peak A experiences destructive interference. According to similar analyses of the preceding electric field, the largest cutoff is expected to increase by enhancing $\sqrt{R}$ value, whereas the second-largest cutoff would remain invariable. Figure 5(c) shows the HHG spectrum when $\sqrt{R}$ is set to be 0.6; a wide 300-eV continuum is directly obtained on HHG spectrum. A time-frequency analysis profile in Fig. 6(a) reveals the physical reason for such a wide continuum. By supposing a stronger half-harmonic control pulse, the main burst emission around $t=0$ become sharper and much higher than the two neighboring burst emissions. The enlargement between the height of neighboring peaks induces the extension of the width of continuum.

For an accurate understanding of the continuum bandwidth's dependence on $\sqrt{R}$, we perform our quantum wave-packet code LZH-DICP; the intensity of the harmonics is
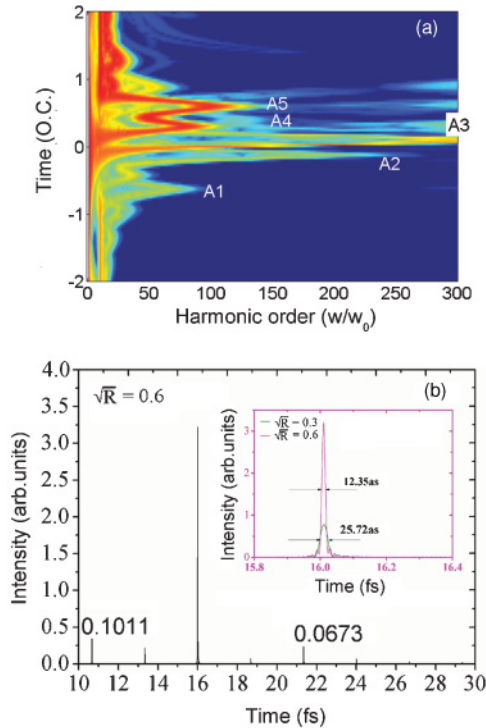
FIG. 6. (Color online) (a) Time-frequency profile (colors are in logarithmic scale) of the HHG power spectra when $\sqrt{R}$ is 0.6. (b) The temporal profiles of the attosecond trains generated when the strength ratio $\sqrt{R}$ is 0.6. Laser parameters in the simulation are as follows. Fundamental pulse, 800 nm, 6 fs, 6×10^{14} W/cm^2; control pulse, 1600 nm, 12 fs, phase = 0, and $\sqrt{R} = 0.6$. The inset shows temporal profiles of the isolated attosecond pulse produced under the half-harmonic control when $\sqrt{R} = 0.3$ and $\sqrt{R} = 0.6$.

represented in the function of the harmonic order and $\sqrt{R}$ in Fig. 5(b). In this case, strength of fundamental pulse is kept constant at 0.1315 a.u. ($I = 6\times10^{14}$ W/cm^2). By varying the relative strength ratio $\sqrt{R}$ from 0 to 0.6 evenly, it is shown clearly that the largest cutoff increase linearly with the relative strength ratio $\sqrt{R}$. The result is consistent with the heterodyne mixing theory proposed by Pfeifer *et al.* [21] and again implies that the effect brought by the half-harmonic control could substitute the requirement for improving driving pulse's condition to some extent.

Under the assumption that the chirp of the xuv continuum can be compensated for, we synthesize the harmonics from the continuum by taking Fourier transformation. In Fig. 6(b), an attosecond train can be synthesized by Fourier transforming the harmonics from the 300-eV continuum shown in Fig. 5(c). It is worth noting that this pulse train can be treated as an

isolated attosecondpulse, since the strength of the second-largest attosecond pulse is only equal to 0.1011 of the strength of the main pulse. The inset in Fig. 6(b) shows an isolated attosecond pulse lasting 25.72 as which is created by Fourier transforming 83 to the 174 harmonic when $\sqrt{R}$ is equal to 0.3. By increasing $\sqrt{R}$ further into 0.6, an isolated 12.35-attosecond pulse which meets the Fourier transform limit can be theoretically predicted by synthesizing the continuous harmonic range which is from 105 to 300 harmonic.

IV. CONCLUSION

In conclusion, we theoretically investigated the generation of continuum with wide spectral width in a two-color scheme with different laser parameters. In this work, both classical and quantum analyses are carried out and support our results consistently. First, the three schemes, without control, second-harmonic control, and half-harmonic control, have been compared. Results indicate that the "half-harmonic control" is a more promising way of generating wider continuum. Second, under the half-harmonic control, the continuum of HHG spectra shows sensitive dependence on the relative phase and widest continuum on HHG spectrum is achieved when the relative phase is around zero. Third, under half-harmonic control, the continuum bandwidth display a linear dependence on the relative strength ratio of the CP, which is consistent with heterodyne mixing theory proposed by Pfeifer *et al.* Unlike other work, our research does not consider CEP, polarization angle, or other physical effects on the HHG process and ignores the actual capability of laboratories to some extent. Nevertheless, infrared (ir) control pulse such as half-harmonic control's property as well as the finding of empirical rules in generating the shortest attosecond pulse under half-harmonic control is our focus. Finally, using a 6×10^{14} W/cm^2 800-nm fundamental pulse, mixing a half-harmonic control pulse with relative strength ratio 0.6 and zero phase shift, it is demonstrated that a 300-eV continuum supporting an isolated 12-as pulse can be produced. Utilizing such a short attosecond pulse, researchers are able to measure and control the ultrafast electron dynamics with an unprecedented time resolution.

[1] M. Uiberacker *et al.*, Nature (London) **446**, 627 (2007).

[2] R. Kienberger *et al.*, Nature (London) **427**, 817 (2004).

[3] P. Agostini and L. F. DiMauro, Rep. Prog. Phys. **67**, 813 (2004).

[4] T. Brabec and F. Krausz, Rev. Mod. Phys. **72**, 545 (2000).

[5] I. J. Sola *et al.*, Nat. Phys. **2**, 319 (2006).

[6] G. Sansone *et al.*, Science **314**, 443 (2006).

[7] G. Sansone, Phys. Rev. A **79**, 053410 (2009).

[8] G. Sansone *et al.*, Phys. Rev. A **80**, 063837 (2009).

[9] Y. L. Yu *et al.*, Phys. Rev. A **80**, 053423 (2009).

[10] Z. H. Chang, Phys. Rev. A **76**, 051403 (2007).

[11] S. Gilbertson, Y. Wu, S. D. Khan, M. Chini, K. Zhao, X. M. Feng, and Z. H. Chang, Phys. Rev. A **81**, 043810 (2010).

[12] X. M. Feng, S. Gilbertson, H. Mashiko, H. Wang, S. D. Khan, M. Chini, Y. Wu, K. Zhao, and Z. H. Chang, Phys. Rev. Lett. **103**, 183901 (2009).

[13] E. Goulielmakis *et al.*, Science **320**, 1614 (2008).

[14] T. Pfeifer, L. Gallmann, M. J. Abel, P. M. Nagel, D. M. Neumark, and S. R. Leone, Phys. Rev. Lett. **97**, 163901 (2006).

[15] H. Merdji, T. Auguste, W. Boutu, J. P. Caumes, B. Carré, T. Pfeifer, A. Jullien, D. M. Neumark, and S. R. Leone, Opt. Lett. **32**, 3134 (2007).

[16] B. Kim, J. Ahn, Y. L. Yu, Y. Cheng, Z. Z. Xu, and D. E. Kim, Opt. Express **16**, 10331 (2008).

[17] J. Mauritsson, J. M. Dahlstrom, E. Mansten, T. Fordell, J. Phys. B **42**, 134003 (2009).

[18] H. Xiong, R. X. Li, Z. N. Zeng, Y. H. Zheng, Y. Peng, X. Yang, X. W. Chen, H. P. Zeng, and Z. Z. Xu, Phys. Rev. A **75**, 051802 (2007).

[19] Z. Zhai and X.S. Liu, J. Phys. B **41**, 125602 (2008).

[20] Y. Oishi, M. Kaku, A. Suda, F. Kannari, K. Midorikawa, Opt. Express **14**, 7230 (2006).

[21] T. Pfeifer, L. Gallmann, M. J. Abel, P. M. Nagel, D. M. Neumark, and S. R. Leone, Phys. Rev. Lett. **97**, 163901 (2006).

[22] E. J. Takahashi, T. Kanai, K. L. Ishikawa, Y. Nabekawa, and K. Midorikawa, Phys. Rev. Lett. **101**, 253901 (2008).

[23] X. S. Liu and N. N. Li, J. Phys. B **41**, 015602 (2008).

[24] L. E. Chipperfield, J. S. Robinson, J. W. G. Tisch, and J. P. Marangos, Phys. Rev. Lett. **102**, 063003 (2009).

[25] G. T. Zhang, J. Wu, C. L. Xia, and X. S. Liu, Phys. Rev. A **80**, 055404 (2009).

[26] C. L. Xia, G. T. Zhang, J. Wu, and X. S. Liu, Phys. Rev. A **81**, 043420 (2010).

[27] P. Zou, Z. N. Zeng, Y. H. Zheng, Y. Y. Lu, P. Liu, R. X. Li, and Z. Z. Xu, Phys. Rev. A **81**, 033428 (2010).

[28] W. Y. Hong, P. X. Lu, P. F. Lan, Q. G. Li, Q. B. Zhang, Z. Y. Yang, and X. B. Wang, Phys. Rev. A **78**, 063407 (2008).

[29] C. Vozzi, F. Calegari, F. Frassetto, L. Poletto, G. Sansone, P. Villoresi, M. Nisoli, S. De Silvestri, and S. Stagira, Phys. Rev. A **79**, 033842 (2009).

[30] P. F. Lan, P. X. Lu, Q. G. Li, F. Li, W. Y. Hong, and Q. B. Zhang, Phys. Rev. A **79**, 043413 (2009).

[31] Q. G. Li, P. X. Lu, W. Y. Hong, Q. B. Zhang, and Z. Y. Yang, Phys. Rev. A **80**, 043417 (2009).

[32] Y. H. Guo, R. F. Lu, K. L. Han, and G. Z. He, Int. J. Quantum Chem. **109**, 3410 (2009).

[33] R. F. Lu, H. X. He, Y. H. Guo, Y. H., and K. L. Han, J. Phys. B **42**, 225601 (2009)

[34] R. F. Lu, P. Y. Zhang, and K. L. Han, Phys. Rev. E **77**, 066701 (2008).

[35] T. S. Chu, Y. Zhang, and K. L. Han, Int. Rev. Phys. Chem. **25**, 201 (2006).

[36] K.-L. Han, G.-Z. He, and N.-Q. Lou, J. Chem. Phys. **105**, 8699 (1996).

[37] T.-S. Chu and K.-L. Han, Phys. Chem. Chem. Phys. **10**, 2431 (2008).

[38] K.-L. Han, and G.-Z. He, J. Photochem. Photobiol. C Photochem. Rev. **8**, 55 (2007).

[39] J. Hu, K. L. Han, and G. Z. He, Phys. Rev. Lett. **95**, 123001 (2005).

[40] J. Hu, M. S. Wang, K. L. Han, and G. Z. He, Phys. Rev. A **74**, 063417 (2006).

[41] K. C. Kulander, K. J. Schafer, and J. F. Krause, in *Atoms in Intense Radiation Fields*, edited by M. Gavrila (Academic Press, New York, 1992), Advances in Atomic, Molecular, and Optical Physics, Suppl. 1.

[42] P. B. Corkum, Phys. Rev. Lett. **71**, 1994 (1993).

[43] A. Baltuska *et al.*, Nature (London) **421**, 611 (2003).

[44] J. J. Carrera, X. M. Tong, and S. I. Chu, Phys. Rev. A **74**, 023404 (2006).

[45] X. M. Tong, and S. I. Chu, Phys. Rev. A **61**, 021802 (2000).

[46] X. Chu, and S. I. Chu, Phys. Rev. A **64**, 063404 (2001).

[47] G. W. F. Drake, M. M. Cassar, and R. A. Nistor, Phys. Rev. A **65**, 054501 (2002).

[48] T. Zhang and G. W. F. Drake, Phys. Rev. A **54**, 4882 (1996).

[49] R. El-Wazni and G. W. F. Drake, Phys. Rev. A **80**, 064501 (2009).

[50] P. Antoine, B. Piraux, and A. Maquet, Phys. Rev. A **51**, R1750 (1995).

[51] O. Smirnova, V. S. Yakovlev, and A. Scrinzi, Phys. Rev. Lett. **91**, 253001 (2003).

[52] L. C. Dinu, H. G. Muller, S. Kazamias, G. Mullot, F. Auge, P. Balcou, P. M. Paul, M. Kovacev, P. Breger, and P. Agostini, Phys. Rev. Lett. **91**, 063901 (2003).

[53] J. Mauritsson, P. Johnsson, E. Gustafsson, A. L'Huillier, K. J. Schafer, and M. B. Gaarde, Phys. Rev. Lett. **97**, 013001 (2006).

[54] H. Mashiko, S. Gilbertson, C. Q. Li, S. D. Khan, M. M. Shakya, E. Moon, and Z. H. Chang, Phys. Rev. Lett. **100**, 103906 (2008).

[55] E. Mansten, J. M. Dahlström, P. Johnsson, M. Swoboda, A. L. Huillier and J. Mauritsson, New J. Phys. **10**, 083041 (2008).